Inorganic Chemistry

Article

pubs.acs.org/IC

Reversible Solid State Redox of an Octacyanometallate-Bridged Coordination Polymer by Electrochemical Ion Insertion/Extraction

Masashi Okubo,*[,†] Koichi Kagesawa,[†] Yoshifumi Mizuno,[†] Daisuke Asakura,[†] Eiji Hosono,[†] Tetsuichi Kudo,[†] Haoshen Zhou,*[,†] Kotaro Fujii,[‡] Hidehiro Uekusa,[‡] Shin-ichi Nishimura,[§] Atsuo Yamada,[§] Atsushi Okazawa,[∥] and Norimichi Kojima*[,∥]

[†]National Institute of Advanced Industrial Science and Technology, Umezono 1-1-1, Tsukuba, Ibaraki 305-8568, Japan

[‡]Department of Chemistry and Materials Science, Tokyo Institute of Technology, Ookayama 2-12-1, Meguro-ku, Tokyo 152-8551, Japan

[§]Department of Chemical System Engineering, School of Engineering, The University of Tokyo, Hongo 7-3-1, Bunkyo-ku, Tokyo, 113-8656, Japan

[∥]Graduate School of Arts and Sciences, The University of Tokyo, Komaba 3-8-1, Meguro-ku, Tokyo 153-8902, Japan

Supporting Information

ABSTRACT: Coordination polymers have significant potential for new functionality paradigms due to the intrinsic tunability of both their electronic and structural properties. In particular, octacyanometallate-bridged coordination polymers have the extended structural and magnetic diversity to achieve novel functionalities. We demonstrate that $[Mn(H_2O)][Mn(HCOO)_{2/3}(H_2O)_{2/3}]_{3/4}[Mo(CN)_8]\cdot H_2O$ can exhibit electrochemical alkali-ion insertion/extraction with high durability. The high durability is explained by the small lattice change of less than 1% during the reaction, as evidenced by *ex situ* X-ray diffraction analysis. The *ex situ* X-ray absorption spectroscopy revealed reversible redox of the octacyanometallate. Furthermore, the solid state redox of the paramagnetic $[Mo^{V}(CN)_8]^{3-}$/diamagnetic$[Mo^{IV}(CN)_8]^{4-}$ couple realizes magnetic switching.

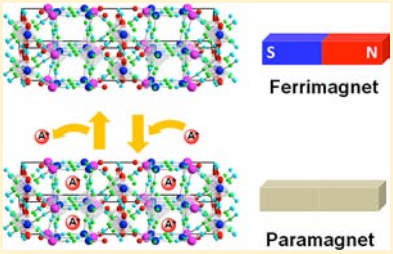

INTRODUCTION

There is currently much interest in functional coordination polymers for technological applications including gas storage,[1] separators,[2] catalysis,[3] sensors,[4] fuel cells,[5] and batteries.[6] The intrinsic tunability of both the electronic and structural properties of these coordination polymers[7−10] provides the potential for improved performance and otherwise novel functionalities.

Compositions such as $A_xM'[M(CN)_6]_{1-y}\cdot\square_y\cdot nH_2O$ (A, alkali metal; M, M′, transition metal; □, $[M(CN)_6]$ vacancy) are known as Prussian blue analogues (PBAs) and are one of the most studied frameworks, because the bridging cyanide ligand has strong σ and π donation/back-donation ability, which underscores the potential for advanced functionalities.[11−13] For example, the strong magnetic exchange interaction between the transition metals through the cyano-bridge has resulted in a room temperature ferrimagnet, $V[Cr(CN)_6]_{0.86}\cdot 2.8H_2O$.[14] The large overlap between the transition metal 3d orbital and the CN 2p orbital also enables metal-to-metal charge transfer, which has realized the $K_{0.3}Co[Fe(CN)_6]_{0.77}\cdot 3.8H_2O$ photomagnet.[15] Furthermore, an electron could move through the overlapping orbitals by thermally activated hopping as polaron, while the guest ion could diffuse through the 3D porous network. These two features provide PBA with mixed conductivity to exhibit the electrochemical ion insertion/extraction expressed as

$$x\mathrm{A}^+ + x\mathrm{e}^- + \mathrm{PBA} \leftrightarrows \mathrm{A}_x\mathrm{PBA}$$

where A^+ is a cation such as Li^+, Na^+, K^+, and NH_4^+.[16−20] During the reaction, the perovskite structure of the PBA is preserved. Magnetic switching has been realized by combining the magnetic and electrochemical properties of PBAs.[21,22]

Recent progress in octacyanometallate-bridged coordination polymers has extended the structural and magnetic diversity of the cyano-bridged coordination polymers, because octacyanometallate complexes $[M^{IV/V}(CN)_8]^{4-/3-}$ (M = Mo, W, Nb) have both topological flexibility due to the higher coordination number, and enhanced magnetic exchange interaction due to the diffused 4d/5d orbital.[23,24] The octacyanometallate-bridged coordination polymers have provided various functionalities (a high T_c magnetism,[25] photomagnetism,[26] magneto-optics[27−29]) with one-, two-, and three-dimensional networks.[30]

The electrochemical solid state reaction of the octacyanometallate-bridged coordination polymers, to the best of our knowledge, has not been reported to date; however, analogous to the PBAs, the cyano-bridged networks with octacyanometallate building blocks are expected to have mixed conductivity for electrochemical ion insertion/extraction.

Received: October 29, 2012
Published: March 11, 2013

Here we demonstrate that the $[Mn(H_2O)][Mn(HCOO)_{2/3}(H_2O)_{2/3}]_{3/4}[Mo(CN)_8]\cdot H_2O$ octacyanometallate-bridged coordination polymer can exhibit electrochemical alkali-ion insertion/extraction with high durability. Control of the valence state accompanied by ion insertion/extraction can realize magnetic switching.

EXPERIMENTAL SECTION

Commercially available chemicals were used without further purification. $Cs_3[Mo(CN)_8]\cdot 2H_2O$ was synthesized by the oxidation of $K_4[Mo(CN)_8]$ according to the literature method.[31]

$[Mn(H_2O)][Mn(HCOO)_{2/3}(H_2O)_{2/3}]_{3/4}[Mo(CN)_8]\cdot H_2O$ was synthesized by a precipitation method. $Cs_3[Mo(CN)_8]\cdot 2H_2O$ (435 mg, 0.6 mmol) in 6 mL of H_2O was added dropwise to $MnCl_2\cdot 4H_2O$ (237 mg, 1.2 mmol) in a mixed solution of 24 mL formic acid and 8 mL H_2O. The precipitate was centrifuged, and then dried in a vacuum at room temperature for 24 h to obtain a dark purple powder (257 mg, 92% yield for Mo). The obtained products were stored under an inert atmosphere in the dark at 5 °C to prevent decomposition. Anal. (%) Calcd for $C_{8.5}H_{5.5}Mn_{1.75}N_8O_{3.5}Mo$: C, 21.82; H, 1.19; Mn, 20.55; N, 23.96; Mo, 20.51. Found: C, 21.25; H, 1.27; Mn, 19.3; N, 22.24; Mo, 19.2. IR: ν(CN) = 2136, 2175, and 2203 cm^{-1}.

The chemical composition was determined by the standard microanalytical method for C, H, and N, and inductively coupled plasma mass spectrometry (ICP-MS) for Mn and Mo. IR spectra were obtained on an Fourier transform-IR (FT-IR) spectrometer (Jasco, FT/IR-6200). Powder X-ray diffraction (Bruker, D8 Advance) analysis was conducted using Cu Kα radiation in 0.01° steps over the 2θ range of 10−80°. *Ex situ* XRD patterns were recorded after washing the lithiated/delithiated (in GITT mode) samples with ethanol. Because of the small amount of the lithiated/sodiated samples (*ca.* 5 mg), the signal-to-noise ratio of the *ex situ* XRD patterns is worse than that for the as-prepared powder. The synchrotron powder XRD pattern for the Rietveld refinement was obtained at BL-4B2 of the Photon Factory at the High Energy Accelerator Research Organization, Japan. The wavelength was set to λ = 1.194 821 Å. The Rietveld refinement was conducted using TOPAS-Academic V4.1 software.

For electrochemical measurements, each sample (50 mg) was ground into a paste with acetylene black (13.3 mg) and poly(tetrafluoroethylene) (3.3 mg), then pressed onto the current collector. For Li-ion insertion/extraction, Li metal was used as the reference and counter electrodes, and 1 M $LiClO_4$ ethylene carbonate (EC)/diethyl carbonate (DEC) solution was used as the electrolyte. The cutoff voltages were 4.3 V versus Li/Li^+ for Li-ion extraction and 3.0 V versus Li/Li^+ for Li-ion insertion. For Na-ion insertion/extraction, Na metal was used as the reference and counter electrodes, and 1 M $NaClO_4$ propylene carbonate (PC) solution was used as the electrolyte. The cutoff voltages were 4.0 V versus Na/Na^+ for Na-ion extraction and 2.7 V versus Na/Na^+ for Na-ion insertion. The open circuit voltages were recorded using the galvanostatic intermittent titration technique (GITT) with repetition of slow ion insertion/extraction at 18 mA/g for 10 min followed by interruption for 1 h.

X-ray absorption near-edge structure (XANES) was performed using synchrotron radiation on beamline BL-9C of the Photon Factory. The quantitatively lithiated/delithiated samples were prepared by the GITT, washed with ethanol, and then dried in vacuo. The spectra were recorded in the transmission mode at room temperature under ambient atmosphere. The energy of X-ray was calibrated by using the metal foil. The observed experimental data were analyzed using RIGAKU REX2000.

Direct current magnetic properties were measured using a superconducting quantum interference device (SQUID) susceptometer (Quantum Design, MPMS5S). The magnetic susceptibility was corrected for the core diamagnetism estimated from Pascal's constants and Pauli paramagnetism due to the acetylene black.

Density functional theory (DFT) calculation was carried out with the Gaussian 09 package.[32] The crystallographic parameters from the powder X-ray diffraction analysis were used as the structural data, except for the hydrogen atoms optimized at the HF/LANL2DZ level with constraining the other atoms. The single-point energies of septet and broken-symmetry[33] quintet states were calculated using the B3LYP functional[34] with the 6-31G(d) basis set for C, H, N, and O, the 6-311G(d) basis set for Mn, and the LANL2DZ basis set with LANL2DZ pseudopotential for Mo.[35] The exchange coupling constant J defined as $H = -2\sum J S_i S_j$ was evaluated from the calculated energies (E_{septet} and $E_{quintet}$) by the spin-projected method as[36]

$$J = \frac{E_{quintet} - E_{septet}}{\langle S^2\rangle_{septet} - \langle S^2\rangle_{quintet}}$$

RESULTS AND DISCUSSION

The octacyanometallate-bridged coordination polymer for electrochemical ion insertion/extraction was synthesized by a precipitation method, in which an aqueous solution of $[Mo^V(CN)_8]^{3-}$ was added to a formic acid solution with manganese chloride. Wang et al. have reported that the single crystal grown from the reaction of $[Mo^V(CN)_8]^{3-}$ with Mn^{2+} in formic acid solution is orthorhombic $[Mn_2(HCOO)(HCOOH)][Mo(CN)_8]\cdot H_2O$.[37]

However, the Mn/Mo molar ratio for the precipitated powder was determined to be 1.76 by inductively coupled plasma spectroscopy (ICP), which is much smaller than the expected value (2.0) for the orthorhombic phase. Furthermore, the synchrotron powder X-ray diffraction (XRD) pattern shown in Figure 1 did not agree with the simulated pattern

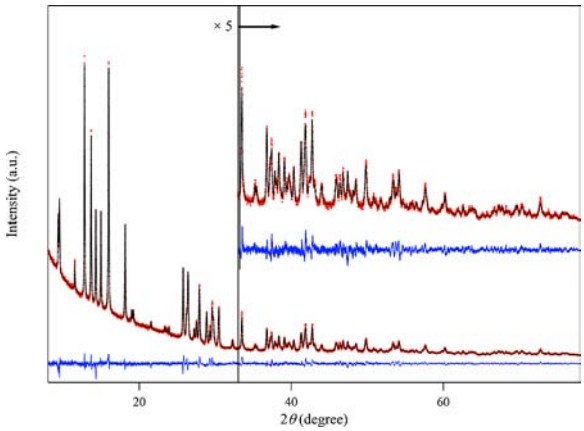

Figure 1. Synchrotron powder X-ray diffraction pattern and Rietveld refinement for MnMo-CCP: measured (red), calculated (black), and difference (blue) data.

for the orthorhombic phase. Wang et al. also reported that, in contrast to $[Mo^V(CN)_8]^{3-}$, $[W^V(CN)_8]^{3-}$ reacted with Mn^{2+} in formic acid solution to crystallize tetragonal $[Mn(H_2O)][Mn(HCOO)_{2/3}(H_2O)_{2/3}]_{3/4}[W(CN)_8]\cdot H_2O$ or orthorhombic $[Mn_2(HCOO)(HCOOH)][W(CN)_8]\cdot H_2O$, depending on the Mn source.[37] While manganese acetate gave the tetragonal phase, manganese perchlorate and manganese chloride gave the orthorhombic phase. Although manganese chloride was used as the Mn source in this study, the powder XRD pattern in Figure 1 could be completely indexed as tetragonal *I*4/*mmm*, which suggests the formation of tetragonal $[Mn(H_2O)][Mn(HCOO)_{2/3}(H_2O)_{2/3}]_{3/4}[Mo(CN)_8]\cdot H_2O$. Formation of the tetragonal phase (expected Mn/Mo = 1.75) was also supported by the Mn/Mo molar ratio determined by ICP.

The Rietveld refinement was conducted using the synchrotron XRD pattern to clarify the crystal structure. The atomic coordinates of $[Mn(H_2O)][Mn(HCOO)_{2/3}(H_2O)_{2/3}]_{3/4}[W-$

dx.doi.org/10.1021/ic302364d | Inorg. Chem. 2013, 52, 3772−3779

$(CN)_8]\cdot H_2O$ from single crystal X-ray crystallographic analysis[37] were used as the initial atomic coordinates. Figure 1 shows the result of Rietveld refinement. The crystal structure was successfully refined with the space group *I*4/*mmm* and a unit cell of a = 7.5739(2) Å, c = 28.8274(7) Å, and V = 1653.7(7) Å^3 (Table S1). The unit cell volume is slightly smaller than that of $[Mn(H_2O)][Mn(HCOO)_{2/3}(H_2O)_{2/3}]_{3/4}[W(CN)_8]\cdot H_2O$ (V = 1671.4(3) Å^3), because the frontier 4d orbital of Mo has smaller radial distribution than the 5d orbital of W. The final R_{wp} and S values were 3.74% and 1.60, and the calculated pattern reproduced the experimental result well, both of which validate the refinement result. Thus, the resulting compound can be characterized as a single phase of tetragonal $[Mn(H_2O)][Mn(HCOO)_{2/3}(H_2O)_{2/3}]_{3/4}[Mo(CN)_8]\cdot H_2O$. Here, it should be mentioned that the proposed composition gives a small discrepancy in the elemental analysis. A possible explanation for this discrepancy is nonstoichiometry such as evaporation of H_2O, defect formation, noncrystalline amorphous impurity, or surface effect, all of which are frequently observed for the cyano-bridged coordination polymers.[11] However, the Rietveld refinement gave a good fit with the proposed structure; thus, the above ideal composition is used in this study for clarity. Hereafter, the compound is denoted as MnMo-CCP (CCP: cyano-bridged coordination polymer).

Figure 2a shows the coordination environment of Mo, Mn1, and Mn2 in MnMo-CCP. Mo has a bicapped trigonal prism geometry (C_{2v}) with three crystallographically independent CN ligands (C1N1, C2N2, and C3N3), all of which bridge between Mo and Mn. Mn1 is coordinated equatorially by 4 N of C2N2, and axially by 1 N of C1N1 and 1 O of H_2O. Mn2 is coordinated equatorially by 4 N of the bridging C3N3 ligand, and axially by 2 O of H_2O and $HCOO^-$. Figure 2b shows the double-deck structure of MnMo-CCP. The bridge between Mo and Mn1 with C2N2 forms a deck plane of a square Mo_2Mn_2 unit in the *ab* plane. The neighboring deck planes are interconnected by bridging between Mo and Mn1 with C1N1 along the *c* axis, which results in the double-deck structure. The neighboring double-deck planes are interconnected by the Mo−C3N3−Mn2−N3C3−Mo linkage to give the 3D cyano-bridged network (Figure 2c). All these structural characteristics of MnMo-CCP are the same as isomorphous $[Mn(H_2O)][Mn(HCOO)_{2/3}(H_2O)_{2/3}]_{3/4}[W(CN)_8]\cdot H_2O$.

The double-deck structure shown in Figure 2b has a 2D open channel in the *ab* plane. PBAs are known to exhibit electrochemical ion insertion/extraction, because the 3D open channel in the cyano-bridged framework provides a 3D ionic diffusion path. Therefore, the 2D open channel in MnMo-CCP is also expected to act as a 2D ionic diffusion path that would permit electrochemical ion insertion/extraction. Therefore, the electrochemical response of MnMo-CCP was tested using cyclic voltammetry (CV). Note that a mean particle size of MnMo-CCP was estimated at about 100 nm by the SEM image (Figure S1).

Figure 3 shows CV curves for MnMo-CCP at 298 K with 1 M $LiClO_4$/ethylene carbonate (EC)−diethyl carbonate (DEC) solution, and 1 M $NaClO_4$/propylene carbonate (PC) solution. Li or Na metal was used as the counterelectrode and reference electrode. The CV curve with the Li^+ electrolyte showed a reversible cathodic peak around 3.37 V with a small shoulder at 3.59 V, and a reversible anodic peak around 3.52 V versus Li/Li^+. The formal potential of the $[Mo^V(CN)_8]^{3-}/[Mo^{IV}(CN)_8]^{4-}$ couple is known to be 0.80 V versus NHE (3.84 V vs Li/Li^+) in 0.25 M KNO_3 aqueous solution;[38] therefore, the observed

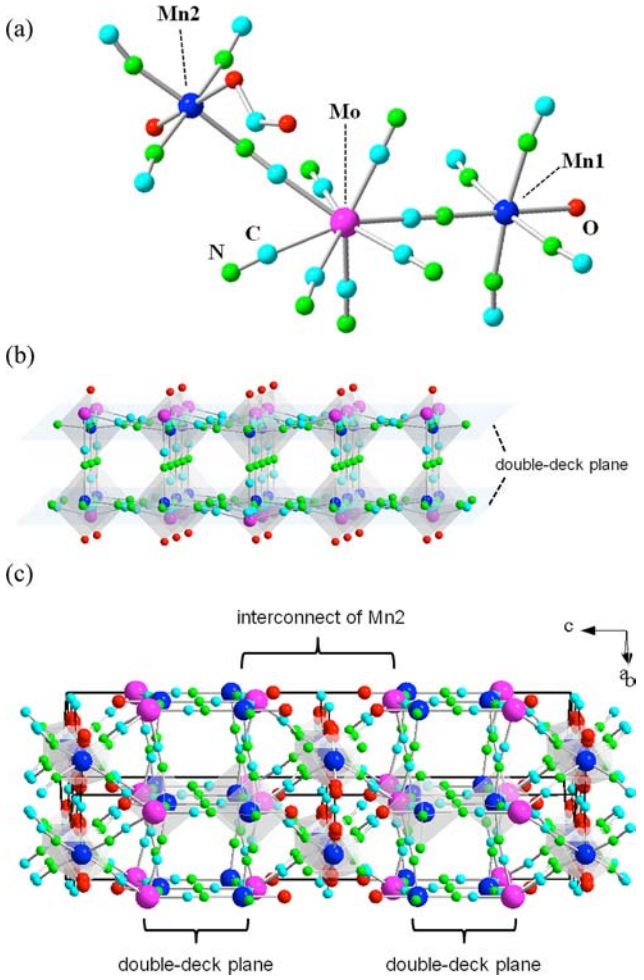

Figure 2. Crystal structure of MnMo-CCP. (a) Coordination environment around Mo, Mn1, and Mn2. (b) Double-deck structure with a 2D ionic diffusion path. (c) 3D network formed by interconnection of the double-deck planes.

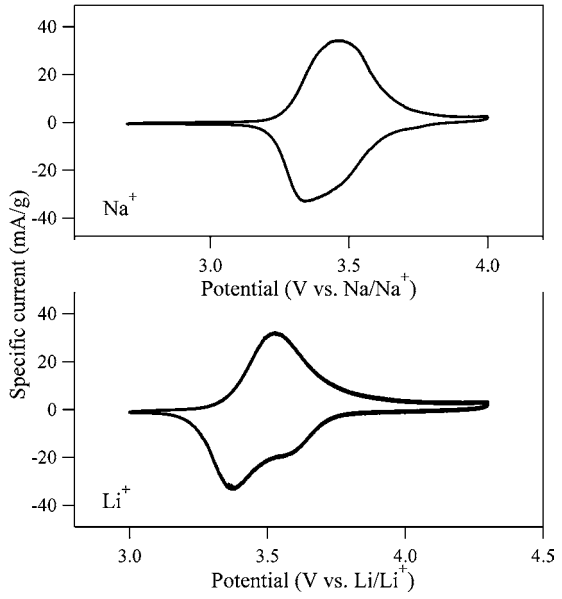

Figure 3. Cyclic voltammograms for MnMo-CCP with 1 M $LiClO_4$/EC−DEC, and 1 M $NaClO_4$/PC. The sweep rate for both cells was 0.1 mV/s.

dx.doi.org/10.1021/ic302364d | *Inorg. Chem.* 2013, 52, 3772−3779

redox potential could be ascribed to the solid state redox of the $[Mo^{V}(CN)_8]^{3-}/[Mo^{IV}(CN)_8]^{4-}$ couple. The peak-to-peak separation ΔE_p between the cathodic and anodic main peaks was 220 mV, which is much larger than that expected for a one-step, one-electron, reversible reaction under a sufficiently slow scan rate. The large ΔE_p could be explained by the slow kinetics of the electrode reaction with respect to the scan rate. The anodic peak may also contain multiple components, although the shoulder component for the anodic scan is not as well resolved as for the cathodic scan, since the polarization of the shoulder component is smaller than that of the main component. This result suggests that the kinetics of the shoulder component is faster than that of the main component. Therefore, it is most likely that the shoulder component is due to the redox of the surface sites, which have higher redox potential than the bulk sites.

The solid state redox of the $[Mo^{V}(CN)_8]^{3-}/[Mo^{IV}(CN)_8]^{4-}$ couple was confirmed by *ex situ* infrared (IR) spectra. The stretching frequency of CN (ν(CN)) is a good measure for the valence state of the coordinated metal, because the d orbital is strongly hybridized with the σ and π orbitals of CN.[39] A higher oxidation state of the metal generally increases ν(CN) due to stronger σ-bonding. The *ex situ* IR spectra (Figure S2) showed that, after electrochemical reduction to 3.0 V vs Li/Li+, the ν(CN) peaks at 2136, 2175, and 2203 cm^{-1} for MnMo-CCP were shifted to lower frequency at 2125 and 2104 cm^{-1}, which indicates that the cathodic/anodic peaks in the CV curves correspond to the solid state redox of the $[Mo^{V}(CN)_8]^{3-}/[Mo^{IV}(CN)_8]^{4-}$ couple.

The CV curve with the Na^+ electrolyte had a cathodic peak around 3.35 V with a small shoulder at 3.51 V, and an anodic peak around 3.46 V versus Na/Na^+. The CV curve is almost identical to that with the Li^+ electrolyte, which could also be ascribed to the solid state redox of the $[Mo^{V}(CN)_8]^{3-}/[Mo^{IV}(CN)_8]^{4-}$ couple. The redox of Mo was also supported by the shift of the ν(CN) in the *ex situ* IR spectra (Figure S2). ΔE_p was 110 mV, which is much smaller than that with the Li^+ electrolyte and could be explained by the fast kinetics of the electrode reaction with the Na^+ electrolyte. The shoulder component for the cathodic scan was also observed with the Na^+ electrolyte, but was not as well resolved as with the Li^+ electrolyte, since the polarization of the main component with the Na^+ electrolyte is smaller than that with the Li^+ electrolyte.

The cathodic/anodic peaks in the CV curves should be ascribed to the electrochemical Li-ion and Na-ion insertion/extraction in MnMo-CCP by analogy with the electrochemical ion insertion/extraction in PBAs. The electrochemical reaction may be described as

$$x\mathrm{A}^+ + x\mathrm{e}^- + \mathrm{MnMo}^{\mathrm{V}}\text{-CCP} \leftrightarrow \mathrm{A}_x\mathrm{Mn}(\mathrm{Mo}^{\mathrm{V}}{}_{1-x}\mathrm{Mo}^{\mathrm{IV}}{}_x)\text{-CCP}$$

if the entire reaction is assumed as a solid solution process. Here, A is Li or Na. The electronic configuration for each metal is expected as $[Mo^{V}(CN)_8]^{3-}$ (d^1, $S = {}^1/_2$), $[Mo^{IV}(CN)_8]^{4-}$ (d^2, $S = 0$), and Mn^{2+} (d^5, $S = {}^5/_2$), respectively.

However, controlled potential methods such as CV cannot determine the true equilibrium potential of the material, and it is also difficult to perform quantitative ion titration into MnMo-CCP to precisely evaluate x. Therefore, an advanced electrochemical characterization technique, i.e., the galvanostatic intermittent titration technique (GITT),[40] was performed; a low-density constant current was repeatedly applied for 10 min, followed by an interruption of 1 h to obtain the open circuit voltage (OCV) at each equilibrium state (Figure S3).

Figure 4 shows the OCVs as a function of x in A_xMnMo-CCP. The amount of inserted/extracted ion x was calculated on

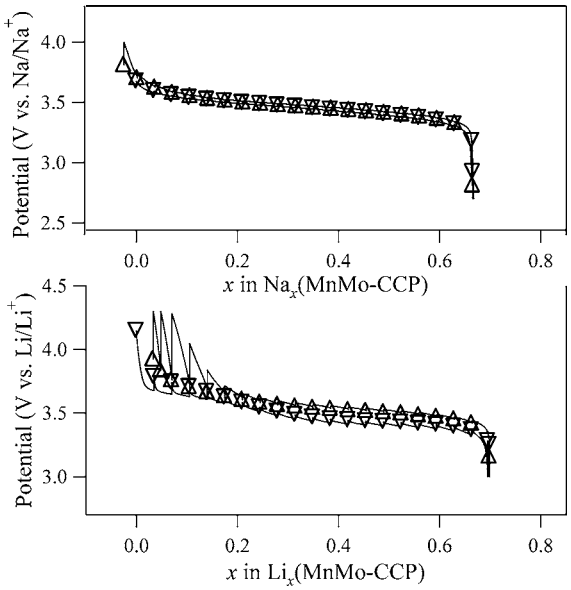

Figure 4. Equilibrium voltage as a function of x for Li_x(MnMo-CCP) and Na_x(MnMo-CCP).

the basis of Faraday's law. The OCVs indicate that 0.7 Li-ion and 0.67 Na-ion could be inserted/extracted reversibly. A dx/dE plot as a function of the potential E clarified that Li-ion insertion/extraction mainly occur at 3.43 and 3.54 V versus Li/Li^+, respectively (Figure S4). Potential hysteresis between the insertion and extraction processes (ca. 110 mV) may be ascribed to polarization within the Li_xMnMo-CCP particles due to slow Li-ion diffusion. In contrast, Na-ion insertion/extraction occurred at 3.46 and 3.47 V, respectively, and the potential hysteresis was negligible (ca. 10 mV), which suggests that polarization is suppressed in Na_xMnMo-CCP particles. The difference in polarization may result from the difference in ionic diffusivity, where Na-ions diffuse faster than Li-ions. The observed redox potentials were in good agreement with those in the CV curves.

The OCV curves suggest that Li-ion or Na-ion insertion may reduce 70% of Mo in MnMo-CCP. In order to confirm the oxidation sate of Mo during the electrochemical reaction, the *ex situ* X-ray absorption near edge structure (XANES) for Mo K-edge was measured for A_xMnMo-CCP (Figure 5). The spectra for $Cs_3Mo^{V}(CN)_8$ and $K_4Mo^{IV}(CN)_8$ are also shown for reference, in which the peak at 20 005.5 eV observed for $Cs_3Mo^{V}(CN)_8$ shifts to 20 004.5 eV for $K_4Mo^{IV}(CN)_8$. The XANES spectra for Li_xMnMo-CCP show that the peak at 20 005.5 eV for MnMo-CCP shifts to 20 004.6 eV for $Li_{0.7}$MnMo-CCP, which confirms the oxidation of Mo. However, the peak position for $Li_{0.7}$MnMo-CCP is slightly higher than that for $K_4Mo^{IV}(CN)_8$; thus, Mo^{V} in MnMo-CCP is not fully reduced by Li-ion insertion, as suggested by the OCV curves. The XANES spectra for Na_xMnMo-CCP also confirm that Mo in MnMo-CCP is redox-active, but is not fully reduced by Na-ion insertion.

Ex situ XRD patterns were recorded for A_xMnMo-CCP to clarify the structural changes during the electrochemical

dx.doi.org/10.1021/ic302364d | *Inorg. Chem.* 2013, 52, 3772−3779

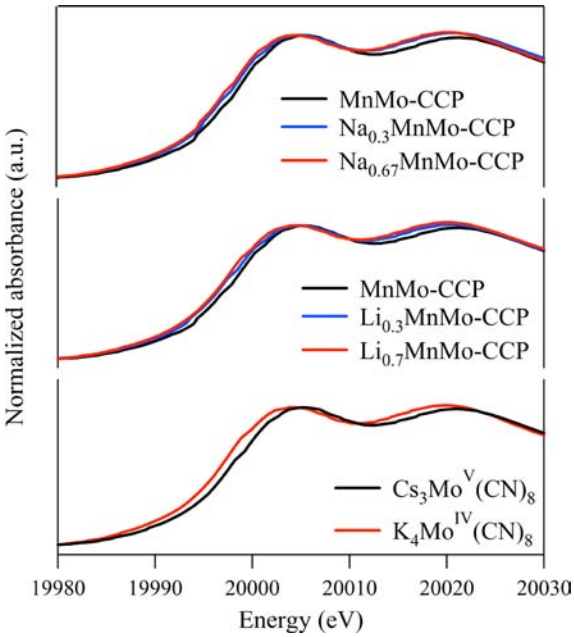

Figure 5. Mo K-edge XANES spectra for $Cs_3Mo^{V}(CN)_8$, $K_4Mo^{IV}(CN)_8$, Li_x(MnMo-CCP), and Na_x(MnMo-CCP).

reaction. Figure 6a shows the XRD patterns for Na_xMnMo-CCP. The diffraction peaks gradually shifted during the entire electrochemical process, and no additional peaks emerged, which suggests that Na-ion insertion/extraction in MnMo-CCP occurs entirely via a solid solution process. Figure 6b shows the calculated unit cell parameters as a function of x in Na_xMnMo-CCP (red triangles). Both the a- and c-axes contracted/expanded reversibly by Na-ion insertion/extraction, while the contraction ratio was 0.5% for the a-axis and 0.7% for the c-axis. This result confirmed the solid solution state of Na_xMnMo-CCP ($0 < x < 0.67$). *Ex situ* XRD patterns for Li_xMnMo-CCP (Figure S5) showed a gradual shift of the diffraction peaks, and the unit cell parameters (Figure 6b, black triangles) also clarified the reversible contraction/expansion of both the a- and c-axes. Therefore, Li-ion insertion/extraction in Li_xMnMo-CCP also occurs via a solid solution process. However, the lattice contraction/expansion of A_xMnMo-CCP is less than 1%, which is much smaller than that for typical Li_xPBA (ca. 3.5%).[20] The small lattice change may be ascribed to the similar bond length of $[Mo^{V}(CN)_8]^{3-}$ (typical Mo^{V}–C bond length from 2.16 to 2.17 Å)[32] and $[Mo^{IV}(CN)_8]^{4-}$ (typical Mo^{IV}–C bond length from 2.15 to 2.17 Å).[26]

It was clarified that MnMo-CCP exhibits reversible electrochemical alkali-ion insertion/extraction. The valence state is changed between the paramagnetic $[Mo^{V}(CN)_8]^{3-}$ (d^1, $S = {}^1/_2$) and diamagnetic $[Mo^{IV}(CN)_8]^{4-}$ (d^2, $S = 0$), so that the magnetism of MnMo-CCP should be switched. Thus, magnetic measurements of A_xMnMo-CCP were performed.

Figure 7a shows the temperature dependence of χT and χ^{-1} for the powder MnMo-CCP. χT at 300 K is 7.04 emu K mol^{-1}, which is smaller than the spin only value (8.03 emu K mol^{-1}). The smaller χT was also reported for the polycrystalline W analogue. One possible explanation for this discrepancy is nonstoichiometry as discussed in the elemental analysis section. χT increased with decreasing temperature, and showed an abrupt increase below 60 K, which suggests a long-range magnetic ordering. The Curie–Weiss fit for χ^{-1} versus T plot above 200 K gave the Curie constant C of 6.77 emu K mol^{-1}

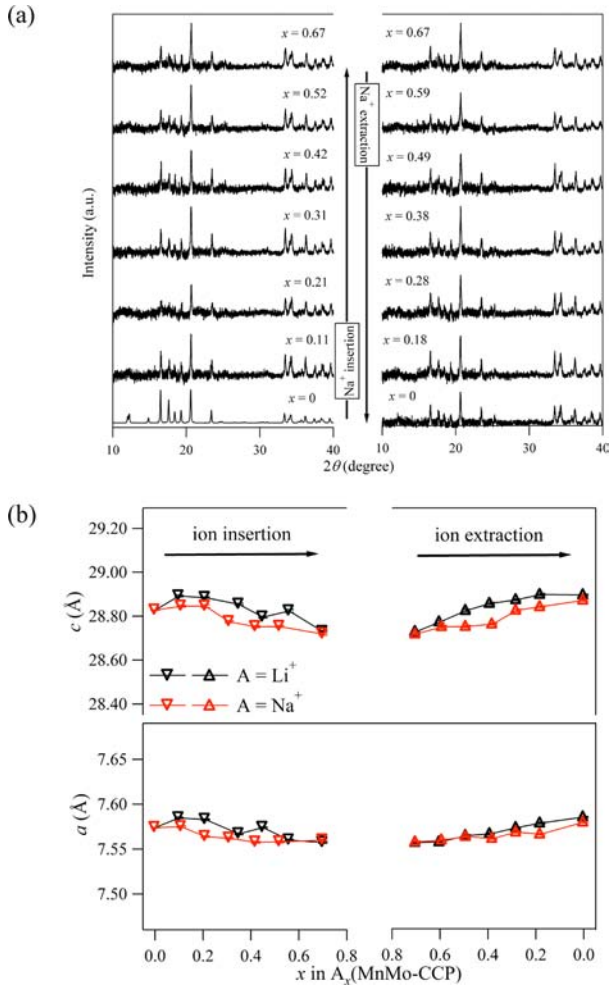

Figure 6. (a) *Ex situ* XRD patterns measured during Na^+ insertion/extraction. (b) Unit cell parameters as a function of x in A_x(MnMo-CCP).

and the positive Weiss constant θ of 13 K, indicating the ferromagnetic character of the dominant interactions in the system.

Figure 7b shows the magnetization M for MnMo-CCP as a function of the magnetic field H at 2 K. M saturated above 5 kOe to 7.35 $N\mu_B$, which is close to the value expected for the ferrimagnetic alignment (7.75 $N\mu_B$) rather than that for the ferromagnetic alignment (9.75 $N\mu_B$). Thus, despite the positive θ, it is most likely that MnMo-CCP shows ferrimagnetic ordering. In connection with the positive θ, it should also be mentioned that there exist two cyrstallographically independent Mn sites in MnMo-CCP, both of which are cyano-bridged to Mo, and no available exact model can treat such a complicated system. Thus, the long-range magnetic ordering suggested by the abrupt increase of χT below 60 K cannot be regarded as ferromagnetic only based on the simple Curie–Weiss law. The magnetic ordering for the W analogue was also regarded as ferrimagnetic based on the saturation magnetization.[37]

According to the previous literature, the magnetic $d_{x^2-y^2}$ orbital of the bicapped trigonal prism $[Mo^{V}(CN)_8]^{3-}$ mainly overlaps with the d_{xy} orbital of Mn^{2+} through the π orbital of CN.[41] The large overlap integral is expected to enhance the kinetic exchange, which provides the antiferromagnetic interaction. To support the ferrimagnetic alignment in MnMo-CCP, we performed the DFT calculation. On the

dx.doi.org/10.1021/ic302364d | *Inorg. Chem.* 2013, 52, 3772–3779

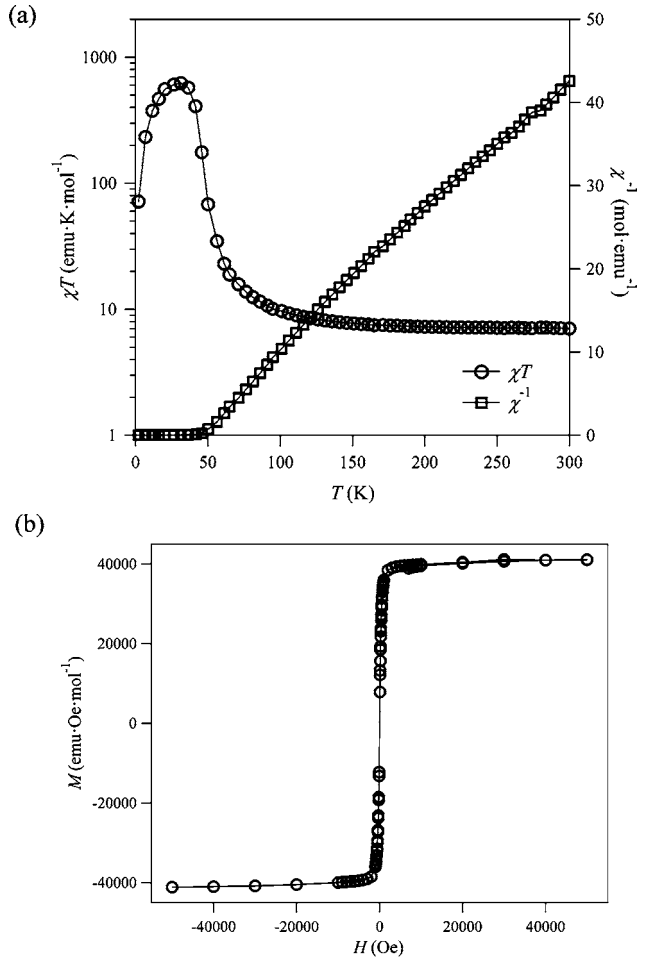

Figure 7. (a) Temperature dependence of χT and χ^{-1}, and (b) the field dependent magnetization for MnMo-CCP.

basis of the structural parameters from the powder X-ray diffraction analysis, the electronic structure was calculated for clusters containing intradeck, interdeck, or interdouble-deck cyano-bridged Mn−Mo pair: $\{(CN)_4(H_2O)Mn\}$−N2C2−$\{Mo(CN)_7\}$, $\{(CN)_4(H_2O)Mn\}$−N1C1−$\{Mo(CN)_7\}$, and $\{(CN)_3(H_2O)_2Mn\}$−N3C3−$\{Mo(CN)_7\}$. Note that there are four and three possible clusters for the intradeck and interdouble-deck pairs because of the disordered cyanides.

Figure 8 shows the calculated spin density for the selected clusters in the quintet state. The other calculated results are shown in Figure S6. The blue and green densities correspond to positive and negative spins. The spin density at Mo for each cluster shows the magnetic orbital characteristics of $d_{x^2-y^2}$ orbital, while that at Mn is spherical due to the high-spin d^5 configuration. The estimated exchange coupling constant $2J$ ranged from −80 to −300 K for the intradeck Mn−Mo pairs, and from −300 to −600 K for the interdouble-deck pairs. As shown in Figure 8, the magnetic $d_{x^2-y^2}$ orbital of Mo in the intradeck and intradouble-deck pairs points toward Mn to provide large overlap integral, which should result in the strong kinetic exchange and antiferromagnetic interaction between Mn and Mo. In contrast, the magnetic exchange is negligible (−2 K) for the interdeck Mn−Mo pair. One possible explanation is that, because the bridging C1N1 points almost perpendicular to the magnetic $d_{x^2-y^2}$ orbital of Mo, no magnetic interaction could arise between two local spins. Another possible explanation is that the kinetic and potential exchanges compensate each other due to orthogonality of the magnetic orbitals, and the septet and quintet states degenerate. Nevertheless, the dominant antiferromagnetic interaction between Mn and Mo is supported by the DFT calculation.

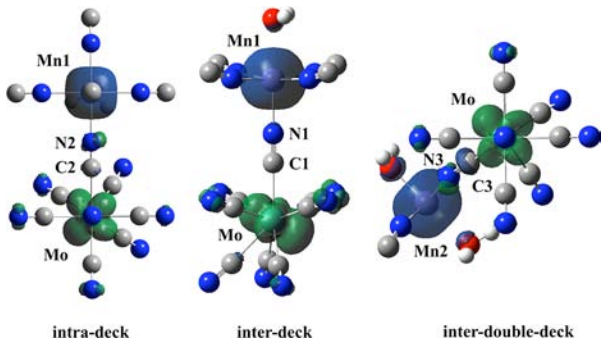

Figure 8. DFT calculated spin density map for selected clusters. The blue and green densities correspond to positive and negative spins, respectively.

Figure 9a shows the temperature dependence of the field cooled (M_{FC}), zero field (M_{ZFC}), and remnant (M_{RM}) magnetization for MnMo-CCP. The abrupt increase of M_{FC} below 46 K confirmed the ferrimagnetic transition. The difference between M_{FC} and M_{ZFC} disappeared above 43 K, which indicates that MnMo-CCP is a ferrimagnet below 43 K. The ferrimagnetic transition temperature T_c of MnMo-CCP is lower than that of isomorphous $[Mn(H_2O)][Mn(HCOO)_{2/3}(H_2O)_{2/3}]_{3/4}[W(CN)_8]\cdot H_2O$ (T_c = 53 K),[37] because the radial distribution of the magnetic 4d orbital of Mo is smaller than that of the 5d orbital of W.

The χT versus T plot for $Li_{0.7}$MnMo-CCP (Figure S7a) was almost constant down to 5 K. This indicates that the ferrimagnetic interaction between Mn and Mo almost disappeared due to the reduction of paramagnetic $[Mo^{V}(CN)_8]^{3-}$ to diamagnetic $[Mo^{IV}(CN)_8]^{4-}$, although 30% of Mo remained as paramagnetic $[Mo^{V}(CN)_8]^{3-}$ in $Li_{0.7}$MnMo-CCP. It should be noted that χT at 300 K is 7.10 emu K mol^{-1}, which is almost the same as that for MnMo-CCP. Since the change in the spin only value is only 3% between MnMo-CCP (8.03 emu K mol^{-1}) and $Li_{0.7}$MnMo-CCP (7.77 emu K mol^{-1}), and some contaminations from the electrolyte are inevitable after the electrochemical treatment, it is difficult to discuss the accurate change in the spin state of Mo in A_xMnMo-CCP based on χT at 300 K.

In Figure 9a (blue open triangles), there was no abrupt increase of M_{FC} for $Li_{0.7}$MnMo-CCP down to 2 K, which suggests the disappearance of the long-range magnetic ordering. Although both M_{FC} and M_{ZFC} showed a slight increase below 10 K, which may be ascribed to local short-range ordering of the Mn and Mo spins due to the 30% paramagnetic Mo, the ferrimagnetic transition was suppressed by Li-ion insertion into MnMo-CCP.

The magnetic properties could be recovered by Li-ion extraction. χT for Li_0MnMo-CCP showed an abrupt increase below 60 K, which suggests the occurrence of the long-range magnetic ordering (Figure S7a). Figure 9a (red plots) shows the temperature dependence of M_{FC}, M_{ZFC}, and M_{RM} for Li_0MnMo-CCP. M_{FC} showed an abrupt increase below 40 K, and the difference between M_{FC} and M_{ZFC} disappeared above 39 K, which indicates that the ferrimagnetic transition is almost reversibly recovered by Li-ion extraction, because diamagnetic

dx.doi.org/10.1021/ic302364d | Inorg. Chem. 2013, 52, 3772−3779

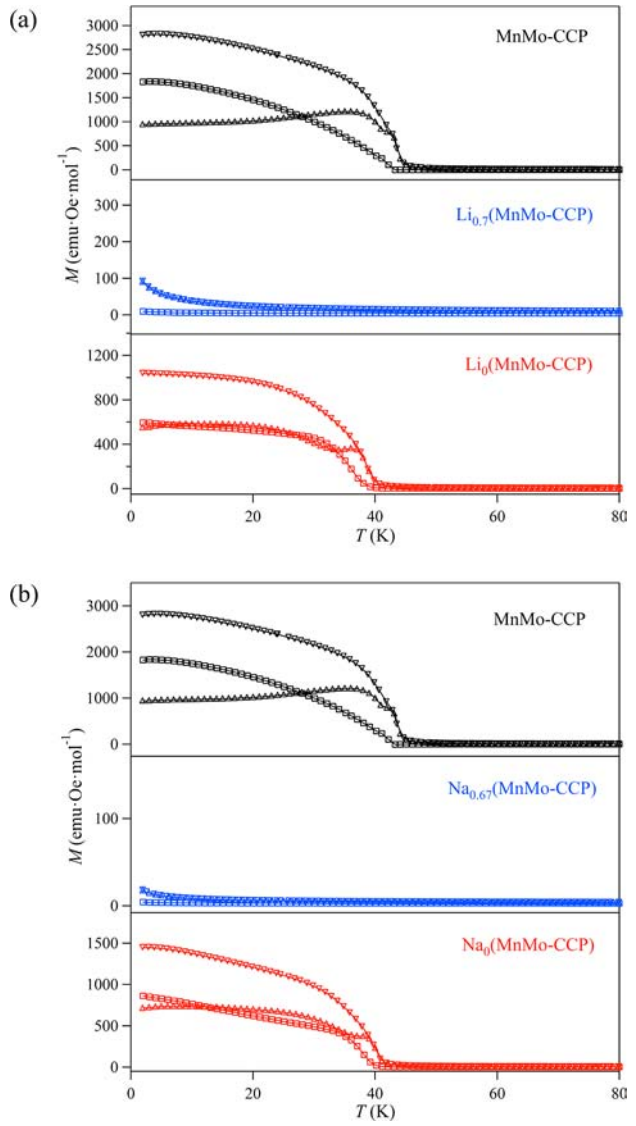

Figure 9. (a) Field cooled (▽), zero field cooled (△), and remnant (□) magnetization for MnMo-CCP (black), $Li_{0.7}$(MnMo-CCP) (blue), and Li_0(MnMo-CCP) (red). (b) Field cooled (▽), zero field cooled (△), and remnant (□) magnetization for MnMo-CCP (black), $Na_{0.67}$(MnMo-CCP) (blue), and Na_0(MnMo-CCP) (red). The notations Li_0(MnMo-CCP) and Na_0(MnMo-CCP) emphasize that the samples were prepared by the electrochemical ion extraction.

$[Mo^{IV}(CN)_8]^{4-}$ is oxidized to paramagnetic $[Mo^{V}(CN)_8]^{3-}$. The T_c of 39 K for Li_0MnMo-CCP is slightly lower than that for MnMo-CCP; therefore, a small amount of diamagnetic Mo may remain in Li_0MnMo-CCP due to slow Li-ion diffusion in the solid. Nevertheless, magnetic switching was successfully achieved by Li-ion insertion/extraction in MnMo-CCP.

The magnetic switching of MnMo-CCP was also achieved by Na-ion insertion/extraction. While χT for $Na_{0.67}$MnMo-CCP was almost constant down to 5 K, χT for Na_0MnMo-CCP increased abruptly below 60 K (Figure S7b). Furthermore, the abrupt increase in M_{FC} disappeared for $Na_{0.67}$MnMo-CCP (blue open triangles), while Na_0MnMo-CCP showed the abrupt increase in M_{FC} (red open triangles), as shown in Figure 9b. These results demonstrate the switching magnetism between a ferrimagnet and a paramagnet by Na-ion insertion/extraction.

Finally, the reversibility of the electrochemical response of MnMo-CCP was evaluated using the constant current method. A specific current of 10 mA/g was applied between cutoff voltages of 3.0 and 4.3 V versus Li/Li^+ for Li-ion insertion/extraction, respectively. The cutoff voltages for Na-ion insertion/extraction were 2.7 and 4.0 V versus Na/Na^+. Potential profiles for Li-ion insertion/extraction showed a reversible potential plateau between 3.7 and 3.2 V versus Li/Li^+, while that for Na-ion insertion/extraction was between 3.6 and 3.2 V versus Na/Na^+ (Figure S8a). Although the shape of the potential profiles were similar to that of the OCV curves in Figure 4, the reversible specific capacity obtained under constant current was ca. 30 mAh/g for both ions, which corresponds to insertion/extraction of 0.52 Li-ion or 0.52 Na-ion. The amount of inserted/extracted ion was slightly smaller than that obtained using the GITT, presumably due to slow ionic diffusion. However, the amount of inserted/extracted ion did not fade over 100 insertion/extraction cycles (Figure S8b), which indicates the robustness of MnMo-CCP against electrochemical alkali-ion insertion/extraction. The high durability of MnMo-CCP can be attributed to the small structural change that occurs during the electrochemical reaction, as confirmed by the *ex situ* XRD results.

■ CONCLUSION

We have described the synthesis, structure, electrochemical response, and switching magnetism of an octacyanometallate-bridged coordination polymer. Structural analysis revealed that the compound has a double-deck structure with a 2D ionic diffusion path. The compound exhibits the electrochemical alkali-ion insertion/extraction, accompanied by the solid state redox of the $[Mo^{V}(CN)_8]^{3-}/[Mo^{IV}(CN)_8]^{4-}$ couple. Both Li-ion and Na-ion insertion/extraction resulted in switching magnetism, i.e., reversible transformation between a ferrimagnet and a paramagnet. The high durability for electrochemical reaction evidenced by the constant current method could be attributed to the small lattice change of less than 1%. The discovery of the novel functionality, i.e., topotactic and durable electrochemical response of the octacyanometallate-bridged coordination polymer, opens a degree of freedom that is not accessible to the classical PBA cyano-bridged coordination polymers.

■ ASSOCIATED CONTENT

Supporting Information

SEM image, *ex situ* IR spectra, GITT experiment, dx/dE vs E plot, *ex situ* XRD patterns, DFT calculated spin density, χT vs T plots, potential profiles, and cycle stability. This material is available free of charge via the Internet at http://pubs.acs.org.

■ AUTHOR INFORMATION

Corresponding Author

*E-mail: m-okubo@aist.go.jp (M.O.); hs.zhou@aist.go.jp (H.Z.); cnori@mail.ecc.u-tokyo.ac.jp (N.K.).

Notes

The authors declare no competing financial interest.

■ ACKNOWLEDGMENTS

Part of this work was financially supported by the Industrial Technology Research Grant Program in 2010 from the New Energy and Industrial Development Organization (NEDO), Japan. M.O. was supported by a KAKENHI on Innovative Areas ("Coordination Programming" Area 2107) from MEXT,

Japan. The synchrotron XRD measurement and the X-ray absorption spectroscopy were conducted under the approval of the Photon Factory Program Advisory Committee (Proposal 2011G196 and 2012G110).

REFERENCES

(1) Farrusseng, D. *Metal-Organic Frameworks: Applications from Catalysis to Gas Storage*; Wiley-VCH: New York, 2011.
(2) Schröder, M. *Functional Metal-Organic Frameworks: Gas Storage, Separation and Catalysis*; Springer-Verlag: New York, 2010.
(3) Seo, J. S.; Whang, D.; Lee, H.; Jun, S. I.; Oh, J.; Jeon, Y. J.; Kim, K. *Nature* **2000**, *404*, 982−986.
(4) Takashima, Y.; Martinez, V. M.; Furukawa, S.; Kondo, M.; Shimomura, S.; Uehara, H.; Nakahama, M.; Sugimoto, K.; Kitagawa, S. *Nat. Commun.* **2011**, *2*, 168.
(5) Rosi, N. L.; Eckert, J.; Eddaoudi, M.; Vodak, D. T.; Kim, J.; O'Keeffe, M.; Yaghi, O. M. *Science* **2003**, *300*, 1127−1129.
(6) Wessells, C. D.; Huggins, R. A.; Cui, Y. *Nat. Commun.* **2011**, *2*, 550.
(7) Farha, O. K.; Yazaydin, A. O.; Eryazici, I.; Malliakas, C. D.; Hauser, B. G.; Kanatzidis, M. G.; Nguyen, S. T.; Snurr, R. Q.; Hupp, J. T. *Nat. Chem.* **2010**, *2*, 944−948.
(8) Shekhah, O.; Wang, H.; Paradinas, M.; Ocal, C.; Schupbach, B.; Terfort, A.; Zacher, D.; Fischer, R. A.; Woll, C. *Nat. Mater.* **2009**, *8*, 481−484.
(9) Ohkoshi, S.; Imoto, K.; Tsunobuchi, Y.; Takano, S.; Tokoro, H. *Nat. Chem.* **2011**, *3*, 564−569.
(10) O'Keeffe, M.; Yaghi, O. M. *Chem. Rev.* **2012**, *112*, 675−702.
(11) Verdaguer, M.; Girolami, G. S. Magnetic Prussian Blue Analogs. In *Magnetism: Molecules to Materials V*; Miller, J. S., Drillon, M., Eds.; Wiley-VCH: New York, 2005; pp 283−346.
(12) Verdaguer, M.; Bleuzen, A.; Marvaud, V.; Vaissermann, J.; Seuleiman, M.; Desplanches, C.; Scuiller, A.; Train, C.; Garde, R.; Gelly, G.; Lomenech, C.; Rosenman, I.; Veillet, P.; Cartier, C.; Villain, F. *Coord. Chem. Rev.* **1999**, *192*, 1023−1047.
(13) Argun, A. A.; Aubert, P. H.; Thompson, B. C.; Schwendeman, I.; Gaupp, C. L.; Hwang, J.; Pinto, N. J.; Tanner, D. B.; Macdiarmid, A. G.; Reynolds, J. R. *Chem. Mater.* **2004**, *16*, 4401−4412.
(14) Ferlay, S.; Mallah, T.; Ouhes, R.; Veillet, P.; Verdaguer, M. *Nature* **1995**, *378*, 701−703.
(15) Sato, O.; Iyoda, T.; Fujishima, A.; Hashimoto, K. *Science* **1996**, *272*, 704−705.
(16) Itaya, K.; Ataka, T.; Toshima, S. *J. Am. Chem. Soc.* **1982**, *104*, 4767−4772.
(17) Itaya, K.; Uchida, I.; Neff, V. D. *Acc. Chem. Res.* **1986**, *19*, 162−168.
(18) de Tacconi, N. R.; Rajeshwar, K.; Lezna, R. O. *Chem. Mater.* **2003**, *15*, 3046−3062.
(19) Wessells, C. D.; Peddada, S. V.; Mcdowell, M. T.; Huggins, R. A.; Cui, Y. *J. Electrochem. Soc.* **2012**, *159*, A98−A103.
(20) (a) Okubo, M.; Asakura, D.; Mizuno, Y.; Kim, J. D.; Mizokawa, T.; Kudo, T.; Honma, I. *J. Phys. Chem. Lett.* **2010**, *1*, 2063−2071. (b) Asakura, D.; Okubo, M.; Mizuno, Y.; Kudo, T.; Zhou, H. S.; Amemiya, K.; de Groot, F. M. F.; Chen, J. L.; Wang, W. C.; Glans, P. A.; Chang, C.; Guo, J.; Honma, I. *Phys. Rev. B* **2011**, *84*, 045117. (c) Mizuno, Y.; Okubo, M.; Asakura, D.; Saito, T.; Hosono, E.; Saito, Y.; Oh-ishi, K.; Kudo, T.; Zhou, H. S. *Electrochim. Acta* **2012**, *63*, 139−145. (d) Asakura, D.; Okubo, M.; Mizuno, Y.; Kudo, T.; Zhou, H. S.; Ikedo, K.; Mizokawa, T.; Okazawa, A.; Kojima, N. *J. Phys. Chem. C* **2012**, *116*, 8364−8369. (e) Nanba, Y.; Asakura, D.; Okubo, M.; Mizuno, Y.; Kudo, T.; Zhou, H. S.; Amemiya, K.; Guo, J.; Okada, K. *J. Phys. Chem. C* **2012**, *116*, 24896−24901.
(21) (a) Okubo, M.; Asakura, D.; Mizuno, Y.; Kudo, T.; Zhou, H. S.; Okazawa, A.; Kojima, N.; Ikedo, K.; Mizokawa, T.; Honma, I. *Angew. Chem., Int. Ed.* **2011**, *50*, 6269−6273. (b) Mizuno, Y.; Okubo, M.; Kagesawa, K.; Asakura, D.; Kudo, T.; Zhou, H. S.; Oh-ishi, K.; Okazawa, A.; Kojima, N. *Inorg. Chem.* **2012**, *51*, 10311−10316.
(22) Sato, O.; Iyoda, T.; Fujishima, A.; Hashimoto, K. *Science* **1996**, *271*, 49−51.
(23) Przychodzen, P.; Korzeniak, T.; Podgajny, R.; Sieklucka, B. *Coord. Chem. Rev.* **2006**, *250*, 2234−2260.
(24) Sieklucka, B.; Podgajny, R.; Korzeniak, T.; Nowicka, B.; Pinkowicz, D.; Koziel, M. *Eur. J. Inorg. Chem.* **2011**, *3*, 305−326.
(25) Imoto, K.; Takemura, M.; Tokoro, H.; Ohkoshi, S. *Eur. J. Inorg. Chem.* **2012**, *16*, 2649−2652.
(26) Hozumi, T.; Hashimoto, K.; Ohkoshi, S. *J. Am. Chem. Soc.* **2005**, *127*, 3864−3869.
(27) Pinkowicz, D.; Podgajny, R.; Nitek, W.; Rams, M.; Majcher, A. M.; Nuida, T.; Ohkoshi, S.; Sieklucka, B. *Chem. Mater.* **2011**, *23*, 21−31.
(28) Koziel, M.; Podgajny, R.; Kania, R.; Lebris, R.; Mathoniere, C.; Lewinski, K.; Kruczala, K.; Rams, M.; Labrugere, C.; Bousseksou, A.; Sieklucka, B. *Inorg. Chem.* **2010**, *49*, 2765−2772.
(29) Long, J.; Chelebaeva, E.; Larionova, J.; Guari, Y.; Ferreira, R. A. S.; Carlos, L. D.; Paz, F. A. A.; Trifonov, A.; Guerin, C. *Inorg. Chem.* **2011**, *50*, 9924−9926.
(30) Sieklucka, B.; Podgajny, R.; Przychodzen, P.; Korzeniak, T. *Coord. Chem. Rev.* **2005**, *249*, 2203−2221.
(31) Dennis, C. R.; van Wyk, A. J.; Basson, S. S.; Leipoldt, J. G. *Transition Met. Chem.* **1992**, *17*, 471−473.
(32) Frisch, M. J.; Trucks, G. W.; Schlegel, H. B.; Scuseria, G. E.; Robb, M. A.; Cheeseman, J. R.; Scalmani, G.; Barone, V.; Mennucci, B.; Petersson, G. A.; Nakatsuji, H.; Caricato, M.; Li, X.; Hratchian, H. P.; Izmaylov, A. F.; Bloino, J.; Zheng, G.; Sonnenberg, J. L.; Hada, M.; Ehara, M.; Toyota, K.; Fukuda, R.; Hasegawa, J.; Ishida, M.; Nakajima, T.; Honda, Y.; Kitao, O.; Nakai, H.; Vreven, T.; Montgomery, J. A., Jr.; Peralta, J. E.; Ogliaro, F.; Bearpark, M.; Heyd, J. J.; Brothers, E.; Kudin, K. N.; Staroverov, V. N.; Kobayashi, R.; Normand, J.; Raghavachari, K.; Rendell, A.; Burant, J. C.; Iyengar, S. S.; Tomasi, J.; Cossi, M.; Rega, N.; Millam, J. M.; Klene, M.; Knox, J. E.; Cross, J. B.; Bakken, V.; Adamo, C.; Jaramillo, J.; Gomperts, R.; Stratmann, R. E.; Yazyev, O.; Austin, A. J.; Cammi, R.; Pomelli, C.; Ochterski, J. W.; Martin, R. L.; Morokuma, K.; Zakrzewski, V. G.; Voth, G. A.; Salvador, P.; Dannenberg, J. J.; Dapprich, S.; Daniels, A. D.; Farkas, Ö.; Foresman, J. B.; Ortiz, J. V.; Cioslowski, J.; Fox, D. J. *Gaussian 09, Revision B.01*; Gaussian, Inc.: Wallingford, CT, 2009.
(33) (a) Noodleman, L. J. *Chem. Phys.* **1981**, *74*, 5737−5743. (b) Noodleman, L.; Davidson, E. R. *Chem. Phys.* **1986**, *109*, 131.
(34) (a) Becke, A. D. *J. Chem. Phys.* **1993**, *98*, 5648−5652. (b) Lee, C.; Yang, W.; Parr, R. G. *Phys. Rev. B* **1998**, *37*, 785.
(35) Hay, P. J.; Wadt, W. R. *J. Chem. Phys.* **1985**, *82*, 270.
(36) Nishino, M.; Yamanaka, S.; Yoshioka, Y.; Yamaguchi, K. *J. Phys. Chem. A* **1997**, *101*, 705.
(37) Wang, T. W.; Wang, J.; Ohkoshi, S.; Song, Y.; You, X. Z. *Inorg. Chem.* **2010**, *49*, 7756−7763.
(38) Sawyer, D. T.; Sobkowiak, A.; Roberts, J. L. *Electrochemistry for Chemists*, 2nd ed.; John & Wiley & Sons, Inc.: New York, 1995.
(39) Nakamoto, K. *Infrared and Raman Spectra of Inorganic and Coordination Compounds*, 6th ed.; John Wiley & Sons, Inc.: New York, 2009.
(40) Weppner, W.; Huggins, R. A. *J. Electrochem. Soc.* **1977**, *124*, 1569−1578.
(41) Song, Y.; Ohkoshi, S.; Arimoto, Y.; Seino, H.; Mizobe, Y.; Hashimoto, K. *Inorg. Chem.* **2003**, *42*, 1848−1856.